Seismic Performance of a River Dike Improved by Sand Compaction Piles

Y. Di[1]; J. Yang, M.ASCE[2]; and T. Sato[3]

Abstract: Sand compaction piling is one of the commonly used countermeasures for earthquake liquefaction hazard of river dikes. This paper presents a case study of the performance of an instrumented dike in northeast Japan that was improved by sand compaction piles and subjected to the 2003 Northern Miyagi Earthquake, with the aim to better understand the effectiveness of this ground improvement method. Simulation has been carried out by means of a fully coupled numerical procedure which employs a sophisticated cyclic elastoplastic constitutive model and the updated Lagrangian algorithm. Comparisons between the field measurements and the computed responses, including the time histories of accelerations and pore-water pressures at different locations, show reasonably good agreement. Numerical simulation has also been made of the same dike but without ground improvement to identify the effects of sand compaction piles in altering the performance of the dike. The study demonstrates that the comprehensive numerical procedure is a promising tool for development of seismic performance-based design of earth structures.

CE Database subject headings: Dikes; Soil liquefaction; Sand; Soil compaction; Seismic effects; Piles.

Introduction

Many river dikes constructed in Japan and China for various purposes such as irrigation and flood control are located in earthquake-prone areas. A great number of case histories have demonstrated that river dikes are highly susceptible to earthquake-induced damage if they are underlain by loose, saturated, noncohesive soils. These soils are frequently found in river environments and have a high liquefaction potential. Hamada et al. (1986, 1996) calculated the vectors of ground displacements by comparing pre- and postearthquake aerial photographs of the 1964 Niigata Earthquake and showed that the liquefied soils of riverbanks resulted in permanent displacements of as large as several meters. Fig. 1 illustrates the typical cross section of a failed embankment and its foundation soil in the 1993 Kushiro-oki, Japan Earthquake along with the photograph of the induced damage (Fudo 1994). The 3–4 m thick peat layer was underlain by a 2–10 m thick alluvial sand layer grading from loose to medium dense and a 20–30 m thick clay layer with thin sand lenses (Sasaki et al. 1995). Liquefaction of river dikes or embankments was also reported for the 1960 Alaska Earthquake (Seed 1970), the 1976 Tangshan Earthquake (Liu et al. 2002), and the 1995 Kobe Earthquake (Matsuo 1996), among many others.

During an earthquake, the shear waves that propagate upward from the underlying bedrock induce the tendency for the loose sandy soil to decrease in volume. If poor drainage conditions are assumed, an increase in pore-water pressure and an equal decrease in the effective confining stress are required to keep the loose sandy soil at constant volume. The degree of excess pore-water pressure build up is largely a function of the initial density and stress state of the soil, and the intensity and duration of seismic shaking. In loose to medium dense sands, pore pressures can be built up to a level that is close to the confining stress. In this state, no effective or intergranular stress exists between the sand grains and a complete loss of shear strength is experienced.

The sand compaction pile (SCP) method, which forms a composite ground by installing piles made of compacted sands into soft ground, has been extensively used to increase the liquefaction resistance of loose sand deposits since the 1970s. The principle of this ground improvement technique is densification of soils. Increases in soil density as well as effective stress are believed to be able to enhance liquefaction resistance of soils. Okamura et al. (2003) reported in situ tests and undrained cyclic shear tests on undisturbed samples obtained by the in situ freezing method at three sites where foundation soils had been improved by sand compaction piles. The results showed that the liquefaction resistance of improved sands was significantly stronger than that of non improved sands. A number of shaking table or centrifuge tests on model embankments (e.g., Elgamal et al. 2002) have also indicated that densification of sand columns is effective in reducing the liquefaction-related deformation.

Although the SCP method as a liquefaction countermeasure has been studied in the laboratory using the element experiments or small-scale model tests, instrumented full-scale tests on its effectiveness are obviously lacking yet much desired. To have a better understanding of the performance of river dikes improved by sand compaction piles, the Japanese National Institute for Land and Infrastructure Management and Kiso-Jiban Consultants Co. Ltd. installed sand compaction piles at a trial dike along the Naruse River, which is located in Nakashita of Miyagi-ken, north-

[1]Assistant Professor, Dept. of Energy and Resources Engineering, College of Engineering, Peking Univ., Beijing, 100871, China.

[2]Assistant Professor, Dept. of Civil Engineering, The Univ. of Hong Kong, Pokfulam, Hong Kong, China (corresponding author). E-mail: junyang@hku.hk

[3]Professor Emeritus, Disaster Prevention Research Institute, Kyoto Univ., Kyoto, Japan.

JOURNAL OF PERFORMANCE OF CONSTRUCTED FACILITIES © ASCE / NOVEMBER/DECEMBER 2008 / **381**

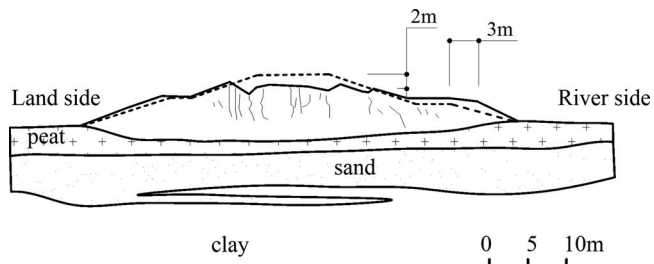J. Perform. Constr. Facil., 2008, 22(6): 381-390

Fig. 1. A failed embankment in the 1993 Kushiro-oki Earthquake (Fudo 1994)

east Japan (Fig. 2). During the 2003 Northern Miyagi Earthquake (Mj 6.4), valuable information on the dynamic response of the dike, including the acceleration and excess pore pressure time histories, was recorded by the installed instruments. This paper presents a study which was aimed at simulating the dike performance by means of a comprehensive, effective stress-based procedure and gaining a better understanding of the effectiveness of sand compaction piles in liquefaction remediation for dikes.

Instrumented Dike and Site Condition

The trial dike is about 6.8 m in height and is made of sandy fills. The dike rests on a Holocene deposit of about 7.0 m. As shown in Fig. 3, the deposit consists of a silty clay layer (Ac1) of 2.2 m, thick sandy layers (Acs and As1) of about 2.6 m, a clay layer (Ac2) of 1.6 m, and a soft rock layer (To). The mean values of the SPT (standard penetration test) blow count number N, shear wave velocity V_s, and unit weight γ of each soil layer as obtained from site investigation are summarized in Table 1 (NILIM-KJC 2004).
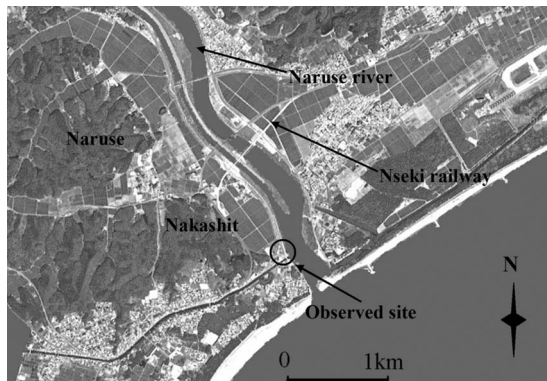

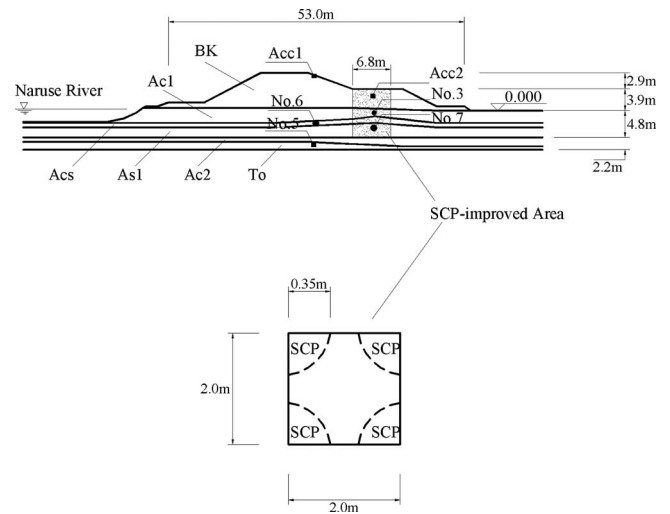**Fig. 2.** Location of the trial dike at the Naruse River

Fig. 3. Cross section of the SCP improved river dike

The SCP-improved zone in the dike is indicated in shadow in Fig. 3. Sand compaction piles were installed below the dike shoulder (on the land side) to a depth of 8.7 m in a square grid pattern, with the diameter of 700 mm and the center-to-center spacing of 2.0 m. The properties of the sand compaction piles were estimated as follows (NILIM-KJC 2004): void ratio 0.7, shear wave velocity 172 m/s, and SPT N value 10.

As shown in Fig. 3, three accelerometers (Acc1, Acc2, and No. 5) were installed in the dike on the land side: one was located at the dike crest (Acc1), one was embedded in the dike shoulder (Acc2), and the third was installed in the soft rock layer (No. 5). To monitor the response of pore-water pressure during earthquakes, three pore-water pressure transducers were installed: two were embedded in the improved zone (No. 3 and No. 7) and one was installed in the sandy soil layer beneath the dike crest (No. 6). During the 2003 Northern Miyagi Earthquake, time histories of acceleration and pore-water pressure were recorded successfully. The peak accelerations recorded by the accelerometer Acc1 in the north–south, east–west, and up–down directions were 379.03, 415.15 and 555.99 gal (cm/s^2) respectively. Table 2 summarizes the peak accelerations recorded by all three accelerometers.

Method of Analysis

Seismic design of dikes or embankments is conventionally conducted by means of the pseudostatic method combined with the Newmark sliding block theory. Although the method provides a simple way of screening for the stability of dikes, it does not adequately account for some situations in real earthquakes (e.g., time-varying amplitudes and frequencies of ground accelerations). In particular, it is unable to provide a reasonable prediction of the permanent deformations associated with the significant buildup of excess pore pressures in liquefiable soils. To quantitatively study the dynamic behavior of earth structures comprising saturated soils, a number of solid–fluid coupled numerical procedures have been developed (see Arulanandan and Scott 1993). These procedures are in general based on the effective stress principle, transient pore fluid movement, generalized material stiffness, and infinitesimal strain theory.

It is now widely recognized, however, that various liquefaction

Table 1. Properties of Soil Layers (Adapted from NILIM-KJC 2004)

Soil layer	Soil type	Elevation (m)	Thickness (m)	SPT-N value (mean)	V_s (m/s)	γ (kN/m^3)
BK	Sandy fill	6.8 to 0.0	6.8	12	150	17
Ac1	Silty clay	0.0 to −2.2	2.2	5	150	14
Acs	Sand	−2.2 to −3.0	0.8	8	150	17
As1	Sand	−3.0 to −4.8	1.8	8	150	17
Ac2	Clay	−4.8 to −6.4	1.6	4	150	18
To	Soft rock	−6.4 to	<-6.4	>50	>650	20

problems involve very large deformations for which the infinitesimal strain theory may not be applicable. To properly describe the large deformation of a soil mass associated with the process of liquefaction, a finite strain procedure has been developed based on the updated Lagrangian algorithm and the two-phase mixture theory (Di and Sato 2004). In this procedure, the Jaumann effective stress rate, an objective measure of the stress rate, is adopted to express the generalized stress–strain relationship, and a finite element and finite difference (FE-FD) hybrid scheme (Oka et al. 1994) is followed to discretize the equilibrium equation and the continuity equation of the fluid-saturated soil. Note that if the mesh is heavily distorted at large deformations, the excess pore pressure field and its gradient cannot, as in a conventional formulation of small strain problems, be reasonably approximated by expressions in terms of the excess pore pressure at the gravity centers of the elements. To handle this problem, the physical area of each element can be divided into subareas, one for each Gauss point, and the pore pressure field in each subarea is assumed to be constant and defined at the Gauss point. More details about the finite strain formulation can be found in Di and Sato (2004).

To adequately reproduce soil behavior under cyclic loading, the elastoplastic constitutive model proposed by Oka et al. (1999) has been adopted in the numerical procedure. This model is based on the nonassociated plasticity and nonlinear kinematic hardening rule. A fading memory characteristic of the initial anisotropy is taken into account in this constitutive relationship. A brief description of this model is given in the Appendix. The model has been carefully evaluated by using a series of hollow-cylinder torsional shear tests with and without an initial shear stress after isotropic and anisotropic consolidation, and has shown a fairly good performance in reproducing the complex soil behavior under various loading conditions (Oka et al. 1999; Matsuo et al. 2000).

Outline of Simulation

The computational model is considered a plane strain problem and restricted to a finite domain (Fig. 4). The maximum horizontal length of the mesh is 690 m, over 50 times the vertical dimen-

sion so that the boundary effect could be minimized. The mesh used for the simulation consists of four-node isoparametric elements with bilinear displacement interpolation and piecewise constant pore-water pressure. All base nodes are conventionally fixed in the vertical direction. Along the two lateral sides of the analysis domain, only vertical displacement is allowed, whereas the horizontal displacement is set to be equal to the free-field displacement. Both the base and the two lateral boundaries are assumed impervious. Ideally, the SCP-improved zone should be modeled in three dimensions by considering the grid pattern of the compaction piles. To avoid complications and for the first instance, it is modeled here as a uniform denser sand zone with higher liquefaction resistance.

Input Motions

The ground accelerations recorded at No. 5 (Fig. 5) can be reasonably assumed to be bedrock motions. It is not considered appropriate, however, to simply take either the acceleration in the east–west component or that in the north–south component as the horizontal input motion for the analysis, in view of the dike orientation (see Fig. 2). The appropriate input motion should be transverse to the river, which can be determined based on the north–south and east–west acceleration components as shown in Fig. 5. In the simulation presented in this paper, the calculated transverse acceleration and the recorded vertical acceleration were used as input motions at the rigid base of the finite element model. A time integration step of 0.001 s was adopted for the dynamic analysis, and the simulation was performed for 80 s.

Model Parameters

The cyclic elastoplastic constitutive model of Oka et al. (1999) was employed for analysis. Table 3 gives soil parameters for the analysis, which were determined using laboratory or field test results, empirical correlations, or set to be typical values of specific soils (typically sandy soil and clay soil). The general principle for the determination of model parameters is outlined as follows. More details about the physical meanings of the model parameters can be found in Oka et al. (1999).

Table 2. Peak Accelerations Observed at Acc1, Acc2, and No. 5 Locations (Adapted from NILIM-KJC 2004)

Position	Peak acceleration (gal.)			
	North–south	East–west	Vertical	Horizontal (transverse to river)
No. 5	578.62	423.82	403.23	443.41
Acc2	370.79	383.20	629.03	363.89
Acc1	379.03	415.15	555.99	402.41
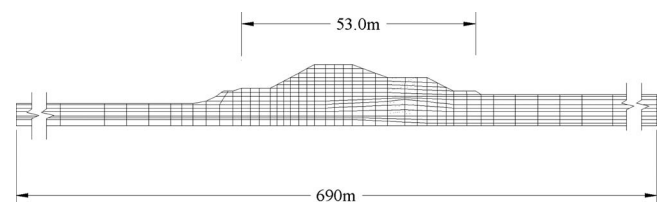
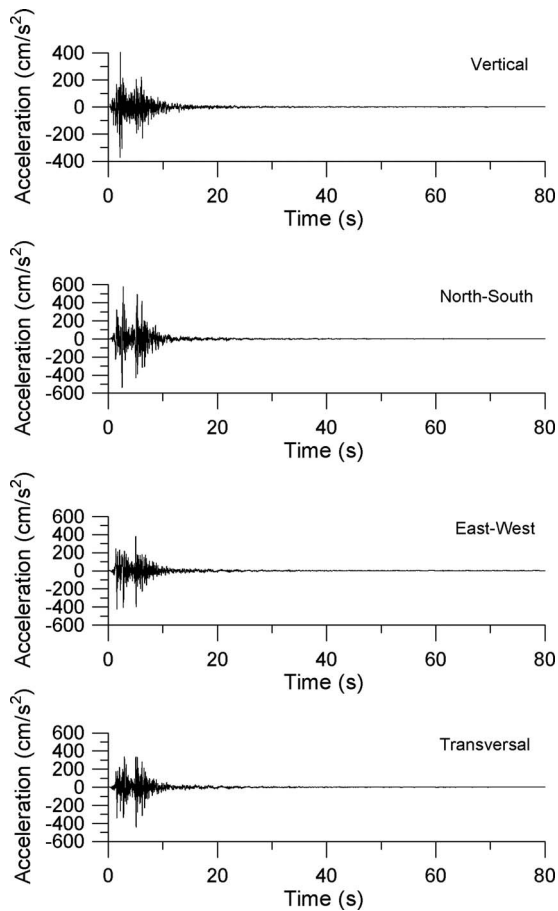**Fig. 4.** Finite-element mesh for the dike

Fig. 5. Acceleration records observed during the 2003 Northern Miyagi Earthquake

The parameters such as density, initial void ratio, and permeability are estimated by physical property tests or set to be typical values of specific soils. The compression and swelling indexes are determined using the compression tests or alternatively set to be
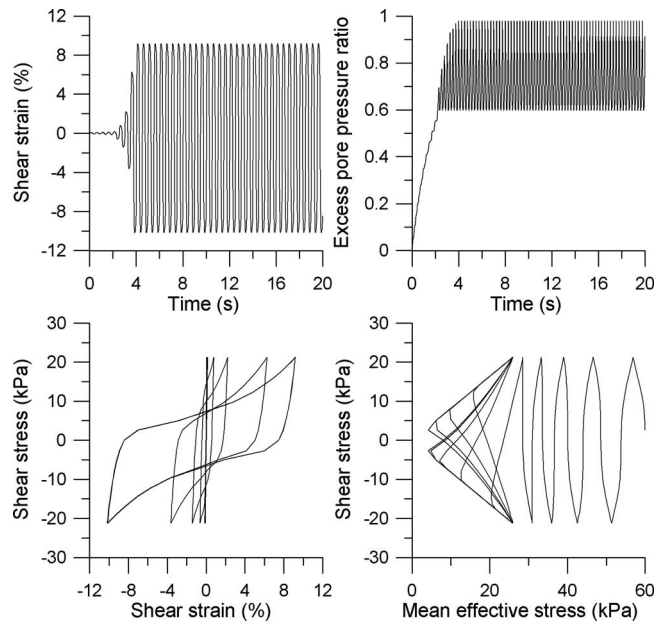

Fig. 6. Model response of the sandy soil (As1) under undrained cyclic loading

typical values of specific soils. The failure stress ratio and the phase transformation stress ratio are estimated from results of undrained triaxial tests. The initial shear modulus is evaluated from the shear wave velocity measured by compression and shear wave (PS) logging or alternatively from the empirical correlation between the shear wave velocity and SPT N value. The remaining parameters are evaluated mainly by matching the results of undrained cyclic tests such as the liquefaction strength curve, the effective stress path, and the stress–strain relation. Note that the parameters D_0 and n mainly control the slope of the liquefaction strength curve, whereas the parameters γ_r^e, γ_r^p control the strain increase after the phase transformation state.

As an example, the simulated behavior of the sand layer (As1) at the cyclic shear stress ratio of 0.33 at a loading rate with a

Table 3. Soil Parameters Used in Analysis

Soil		BK	Ac1	Acs	As1	Ac2	To	SCP-improved zone
Density	$\rho(t/m^3)$	1.70	1.40	1.70	1.70	1.80	2.00	1.70
Coefficient of permeability	$k(m/s)$	1.0E−5	1.0E−8	1.0E−5	1.0E−5	1.0E−8	1.0E−5	1.0E−5
Initial void ratio	e_0	0.90	2.00	0.90	0.90	2.00	0.60	0.70
Compression index	λ	0.02	0.20	0.02	0.02	0.20	0.02	0.02
Swelling index	κ	0.002	0.020	0.002	0.002	0.020	0.002	0.002
Initial shear modulus ratio	G_0/σ'_{m0}	907.0	560.4	635.1	570.2	514.2	9,925.9	837.3
Failure stress ratio	M_f	1.158	1.336	1.158	1.158	1.336	1.510	1.158
Phase transformation stress ratio	M_m	1.013	1.169	1.013	1.013	1.169	1.320	1.013
Hardening parameter	B_0	2,700	1,681	4,000	4,000	1,756	29,778	5,000
Hardening parameter	B_1	135	84	225	225	77	1,489	250
Control parameter of anisotropy	C_d	2,000.0	2,000.0	2,000.0	2,000.0	2,000.0	2,000.0	2,000.0
Reference strain parameter	γ_r^p			0.006	0.006			0.008
Reference strain parameter	γ_r^e			0.04	0.04			0.07
Over consolidation ratio	OCR			1.2	1.2			1.6
Dilatancy parameter	D_0			0.850	0.850			0.415
Dilatancy parameter	η			0.45	0.45			0.41
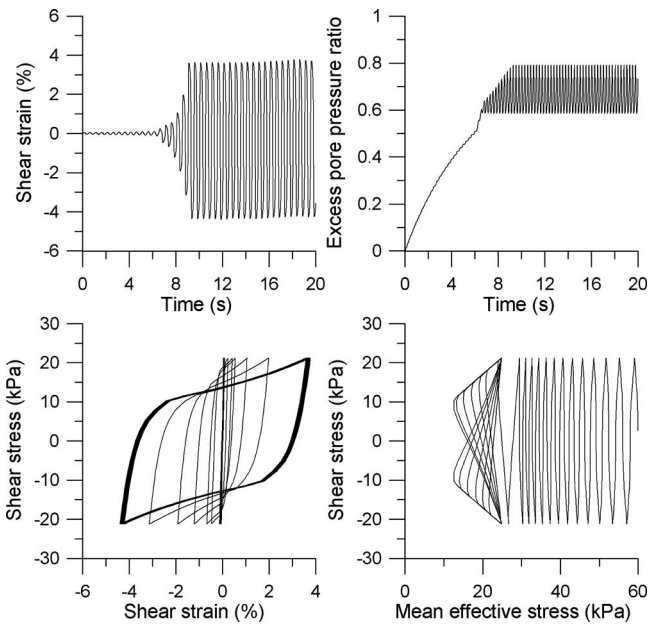
Fig. 7. Model response of the SCP-improved soil under undrained cyclic loading

(a)

(b)

Fig. 8. Deformed mesh of the dike after earthquake shaking: (a) no-improved dike; (b) SCP-improved dike

frequency of 2 Hz is shown in Fig. 6, together with that of the SCP-improved sandy soil at the same shear stress ratio and same loading rate in Fig. 7. The cyclic mobility effect and the reduction of stiffness associated with shear strain upon liquefaction are re-produced reasonably.

Computed Results versus Field Observations

For the purpose of comparison, two parallel numerical simulations have been carried out: one was for the case of the SCP-improved dike and the other was for the case in which the dike was assumed to be nontreated (i.e., without the SCP improvement). Before the dynamic finite element analyses for both cases, a static analysis was performed with gravity to simulate the initial stress acting in situ before the earthquake. The same constitutive model was used in this static analysis.

The deformed mesh of the no-improved dike after earthquake shaking and that of the SCP-improved dike are shown in Fig. 8. The residual deformation is shown by the deformed mesh in solid lines and the original configuration in broken lines. In both cases the deformation pattern followed a common observation that the crest settlement was associated with the lateral spread in foundation soil layers and the lateral spread occurred to both left and right directions. The significant deformation and shear strain occurred in the sandy soil layers under the dike crest (Acs and As1), whereas the upper cohesive soil layer and the dike deformed slightly.

Time histories of the horizontal and vertical displacements at Acc1 and Acc2 are shown in Figs. 9 and 10, respectively. In the case of no-improved dike, the settlement and lateral displacement at Acc1 after the earthquake shaking were about 50 and 30 cm, respectively, and the vertical and horizontal displacements at Acc2 were about 56 and 40 cm, respectively. In the presence of the SCP, the settlement and lateral displacement at both locations were reduced significantly, with the maximum settlement of 28 cm and the maximum horizontal displacement of 8 cm at
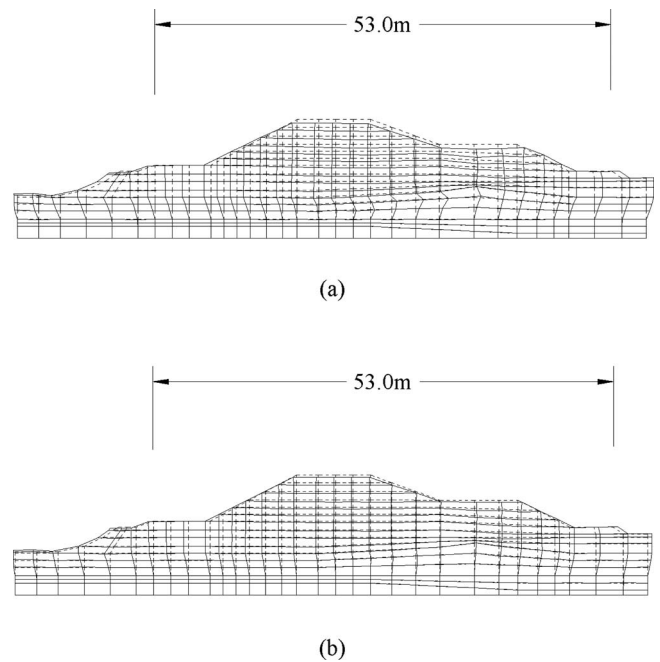
Acc1, and the maximum settlement of 24 cm and the maximum horizontal displacement of 26 cm at Acc2.

The computed time histories of horizontal acceleration and the obtained records at Acc1 and Acc2 locations during the earthquake shaking are shown in Figs. 11 and 12. It can be seen that
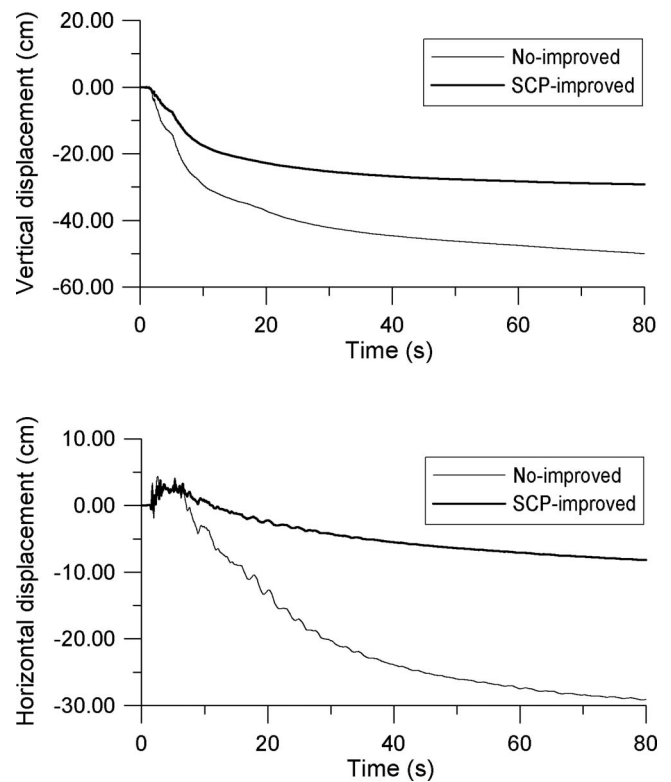

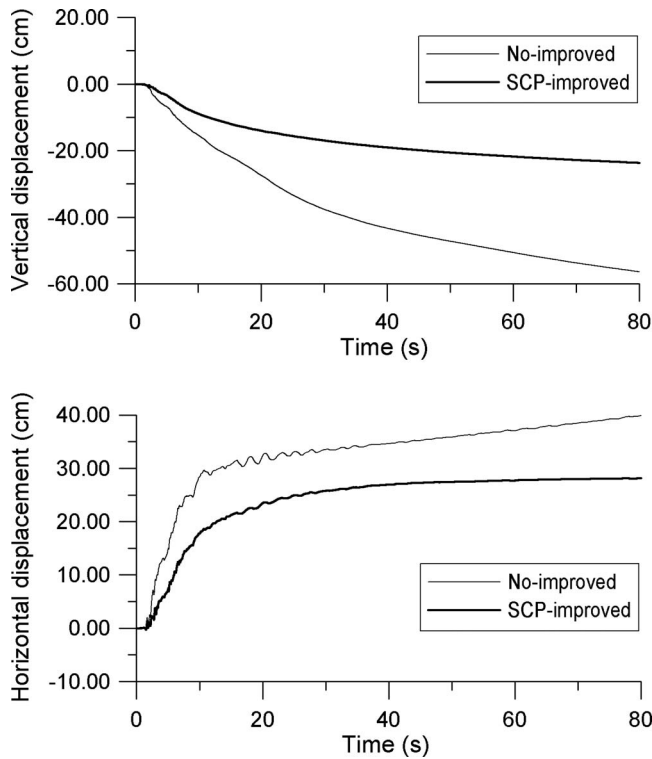**Fig. 9.** Time histories of vertical and horizontal displacements at the Acc1 location

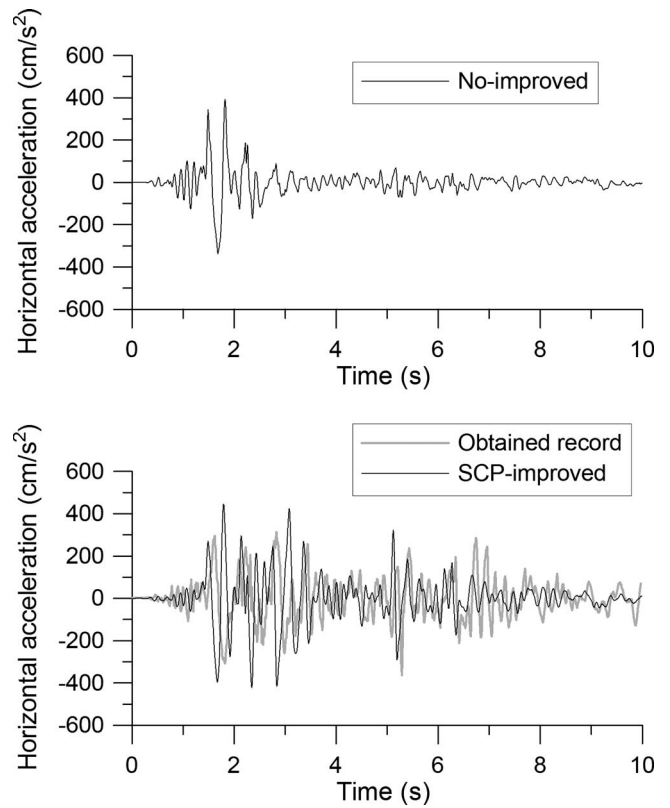**Fig. 10.** Time histories of vertical and horizontal displacements at the Acc2 location
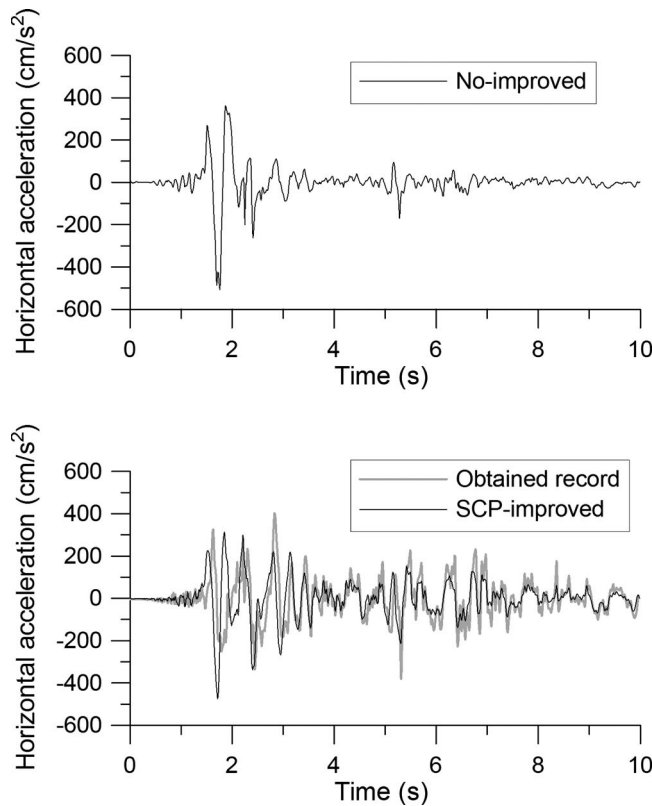

Fig. 12. Time histories of horizontal acceleration at the Acc2 location

the computed acceleration responses at Acc1 and Acc2 for the SCP-improved dike are in fairly good agreement with the records. Note that the horizontal accelerations at Acc1 and Acc2 of the SCP-improved dike were significantly larger than the corresponding ones of the no-improved dike, especially after 3.0 s of shak-
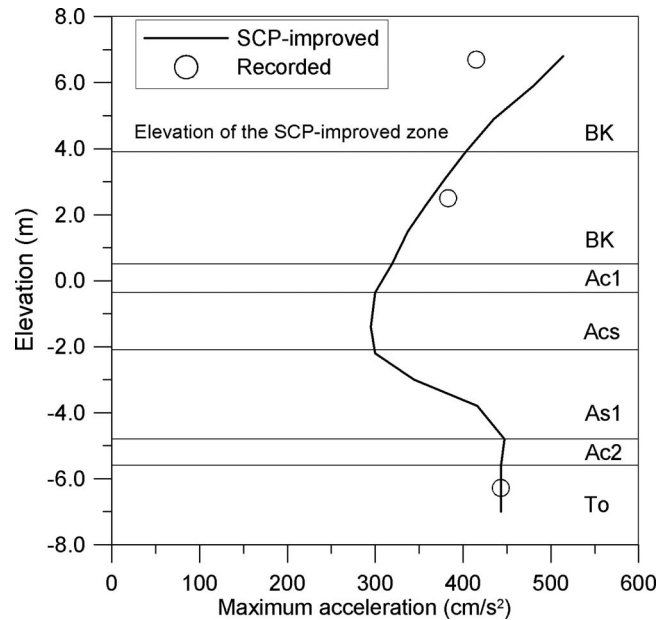

Fig. 11. Time histories of horizontal acceleration at the Acc1 location

Fig. 13. Distribution of peak horizontal acceleration along the vertical direction

386 / JOURNAL OF PERFORMANCE OF CONSTRUCTED FACILITIES © ASCE / NOVEMBER/DECEMBER 2008
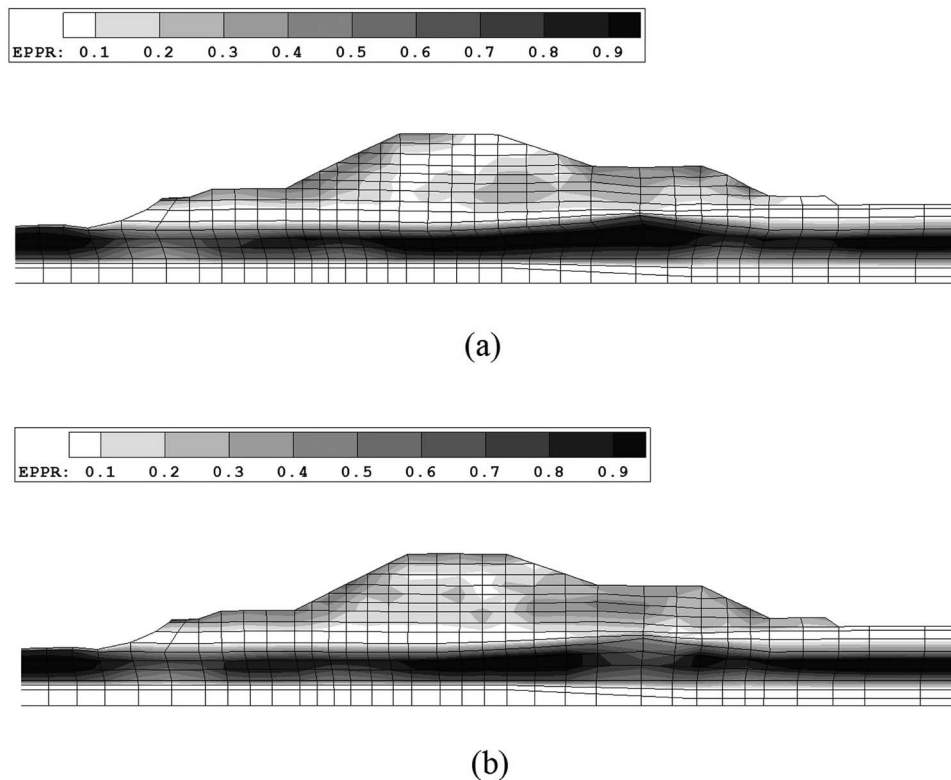
(a)

(b)

Fig. 14. Distribution of excess pore-water pressure ratio after the earthquake: (a) no-improved dike; (b) SCP-improved dike

ing (Fig. 12). This difference is considered, as will be shown later, to be mainly associated with the significant buildup of pore-water pressures in the case of no-improved dike.

Fig. 13 compares the computed distribution of peak horizontal acceleration in the vertical section under the crest of the SCP-improved dike with the recorded distribution, showing an acceptable agreement. Note that the acceleration was deamplified by the sandy layers As1 and Acs, which liquefied in earthquake shaking, but tended to be amplified when the shear waves further propagated toward the dike crest. The deamplification of ground acceleration due to soil liquefaction has been well documented by some downhole array records (Yang et al. 2000).

To have a better view of the pore-water pressure response, Fig. 14 compares the distribution of excess pore-water pressure ratio in the no-improved dike with that of the SCP-improved dike. The grey scale varying from black to white represents the excess pore pressure ratio varying from 1.0 (full saturation) to 0.0. In addition, the computed time histories of excess pore-water pressures at three different locations (No. 3, No. 6, and No. 7) during shaking are shown in Fig. 15, together with the recorded pore-water pressures.

The computed responses of pore-water pressures at No. 3 and No. 7 are apparently consistent with the effective stress paths experienced by the soils as shown in Figs. 16 and 17 (J_2=second invariant of deviatoric stress). The effective stress cyclic elastoplastic constitutive model employed in this paper was developed based on the triaxial test results. To generalize the expression of stress path of saturated soil to other conditions than triaxial test, $\sqrt{2J_2}$ was used as a representation of shearing resistance of the soil. Obviously, for the no-improved dike the pore-water pressures at No. 3 and No. 7 were both built up to the levels of the initial effective mean stresses at the two locations, the corresponding stress path shows a gradual loss of shear strength and a gradual decrease in effective confinement due to excess pore pressure build up, implying that soil liquefaction occurred. By comparison, for the SCP-improved dike, the pore-water pressures at the same locations were still far below the corresponding initial effective mean stresses, the associated stress path shows instantaneous regains of shear strength and confinement due to dilative response of the densified material in SCP-improved zone. The different pore pressure responses were closely associated with the observation described before that the SCP-improved dike exhibited a relatively small lateral spread and crest settlement.

As far as the pore-water pressure at location No. 6 is concerned, (Fig. 18) the computed results do not show a good agreement with the records. Unlike the simulation, the measured excess pore-water pressure did not reach the initial effective mean stress level (about 62 kPa) at location No. 6. If the measured excess pore-water pressure was exact, the soil would not lose the effective mean stress completely and would keep sufficient shear strength. However the investigation after the earthquake shows the occurrence of complete liquefaction in this zone. Therefore, the recorded excess pore-water pressures at these locations might have been the result of an inappropriate measurement. There exist a number of factors that may contribute to the observed discrepancy (e.g., uncertainties of the initial effective mean stress level). The following are thought to be the main possible reasons. In real situations, earthquake shaking induced cracks around the transducer in soils that propagated toward the ground surface and these cracks could certainly reduce the pore-water pressures registered by the transducer. In the numerical simulation, however, the real-life occurrence of cracks could not be reproduced. It points to the limitations of the analytical tool in accounting for the complexity of the real dike behavior and the need to improve the tool.
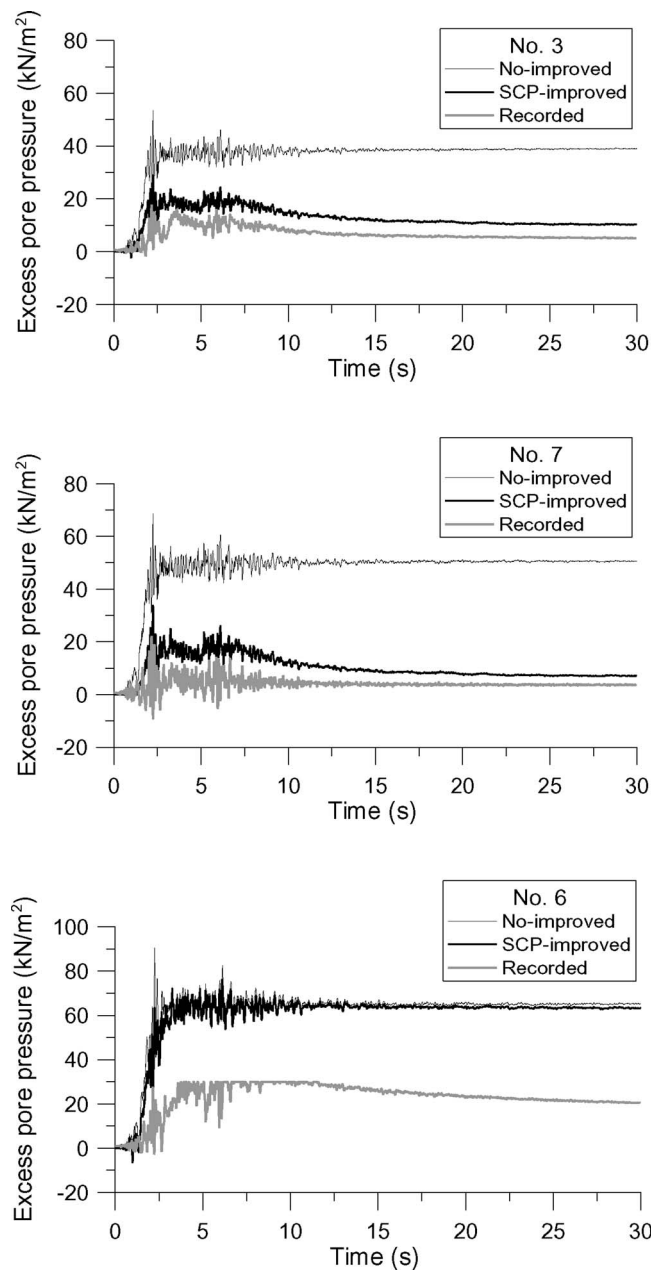
Fig. 15. Time histories of excess pore-water pressure: (a) No. 3 location; (b) No. 7 location; and (c) No. 6 location

Fig. 16. Simulated effective stress path at No. 3 location

Conclusions

A case study has been presented of an instrumented river dike that was improved by sand compaction piles and subjected to the 2003 Northern Miyagi Earthquake. To capture the complex behavior of the river dike involving a significant buildup of pore-water pressures in the underlain sandy soils, simulation has been carried out by means of a fully coupled numerical procedure which employs an effective stress cyclic elastoplastic constitutive model and the updated Lagrangian algorithm. The simulated dike responses, including the time histories of accelerations and pore-water pressures at different locations, generally agree with the observations. The comparisons between the observed and simulated performances (for both the SCP-improved dike and the no-improved dike) may allow the following conclusions.

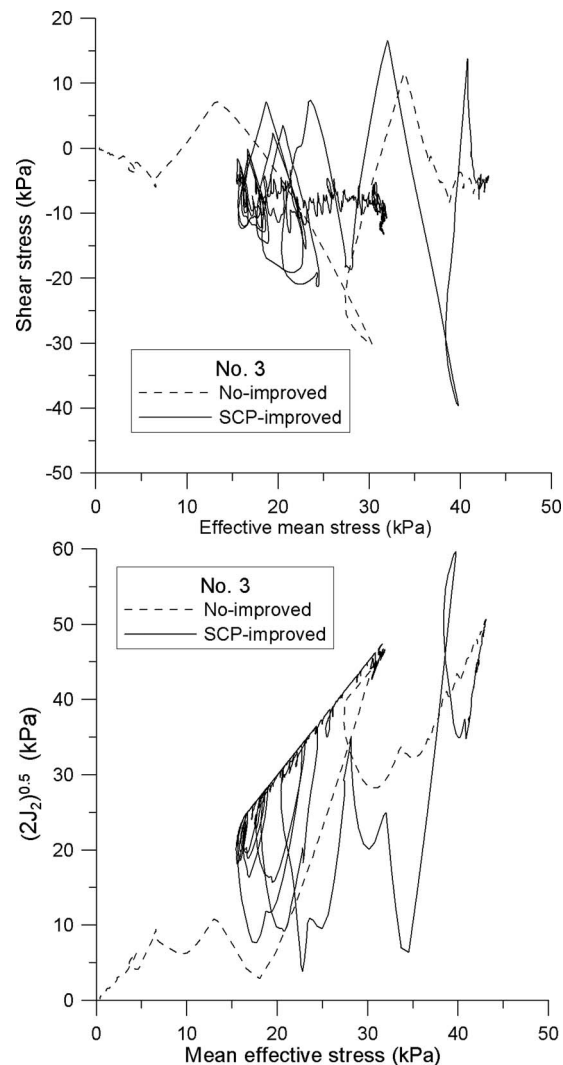1. The densification caused by sand compaction piles was ef-

fective in reducing the crest settlement and lateral spread of the dike associated with the liquefaction of sandy soils beneath the dike. The pore-water pressures recorded by the transducers embedded in the improved zone were significantly lower than the corresponding effective mean stresses.

2. The deformation pattern of the dike was generally characterized by the settlement of dike crest and the associated lateral spread in foundation soil layers. The lateral spread occurred in both the left and right directions.

3. The amplitude of horizontal acceleration was reduced when seismic shear waves propagated through the liquefied soil layers but tended to be increased when waves further traveled toward the dike crest. Compared with the no-improved case, the acceleration at the crest of the SCP-improved dike would exhibit larger amplitudes.

4. The fully coupled large deformation procedure proved to be a promising tool that can provide a reasonable prediction of the seismic performance of real dikes. To improve the prediction accuracy on the one hand and to avoid significant complications on the other hand, further work is needed, particularly with respect to the capability and simplicity of the constitutive model.
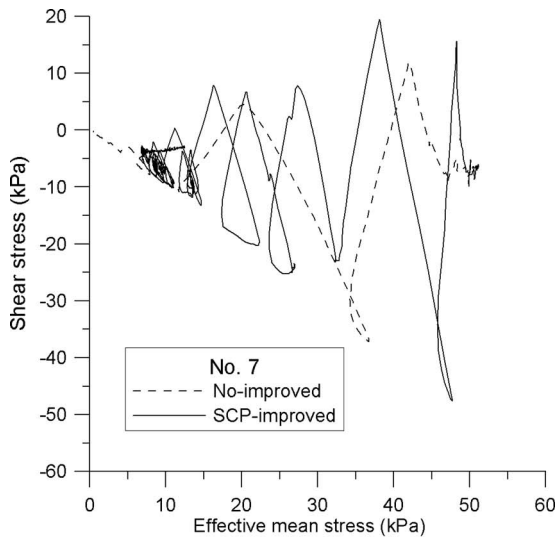
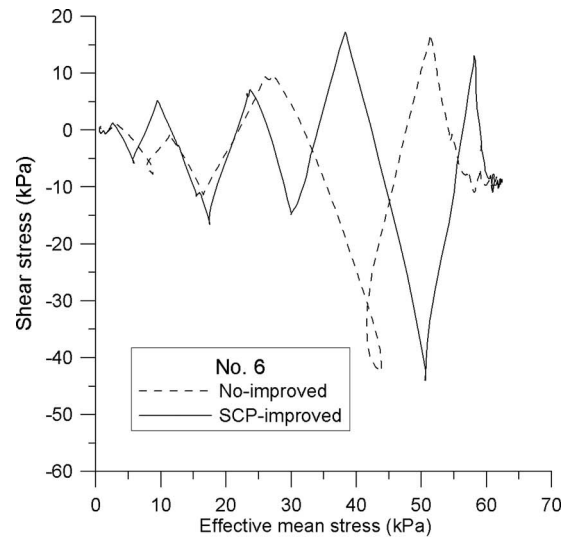**Fig. 17.** Simulated effective stress path at No. 7 location

Fig. 18. Simulated effective stress path at No. 6 location

Acknowledgments

Appendix

The constitutive model is based on the nonassociated plasticity and nonlinear kinematic hardening rule. The boundary surface between the normally consolidated region ($f_b \geq 0$) and the overconsolidated region ($f_b < 0$) is defined by

$$f_b = \bar{\eta}_{(0)} + M_m \ln(\sigma'_m/\sigma'_{mb}) = 0 \tag{1}$$

$$\bar{\eta}_{(0)} = \sqrt{(\eta_{ij} - \eta_{ij(0)})(\eta_{ij} - \eta_{ij(0)})} \tag{2}$$

$$\eta_{ij} = s_{ij}/\sigma'_m \tag{3}$$

where s_{ij}=deviatoric stress tensor; σ'_m=mean effective stress; σ'_{mb}=mean effective stress at the intersection of the overconsolidation boundary surface and the σ'_m axis; $\eta_{ij(0)}$ denotes the value of η_{ij} at the end of anisotropic consolidation, and M_m=phase transformation stress ratio (the value of the stress ratio expressed by $\sqrt{\eta_{ij}\eta_{ij}}$ when the maximum volumetric strain during the shearing occurs).

The σ'_{mb} in Eq. (1) is expressed as

$$\sigma'_{mb} = \sigma'_{mbi} \exp(\nu^p(1 + e_0)/(\lambda - \kappa)) \tag{4}$$

where σ'_{mbi}=initial value of σ'_{mb}; e_0=void ratio; λ=compression index; κ=swelling index; and ν^p=volumetric plastic strain.

The yield surface function of the constitutive model is decided by

$$f = \sqrt{(\eta_{ij} - \chi_{ij})(\eta_{ij} - \chi_{ij})} - R = 0 \tag{5}$$

where R=parameter which defines the elastic region and χ_{ij} =nonlinear kinematic hardening tensor.

The evolution equation for the hardening parameter χ_{ij} is given by

JOURNAL OF PERFORMANCE OF CONSTRUCTED FACILITIES © ASCE / NOVEMBER/DECEMBER 2008 / **389**

J. Perform. Constr. Facil., 2008, 22(6): 381-390

$$d\chi_{ij} = B(M_f \mathrm{de}_{ij}^p - \chi_{ij} d\gamma^p) \qquad (6)$$

where B=material parameter; M_f=stress ratio at failure; de_{ij}^p =increment of the plastic deviatoric strain; and $d\gamma^p = \sqrt{\mathrm{de}_{ij}^p \mathrm{de}_{ij}^p}$.

The parameters B is considered to follow an equation as follows:

$$B = (B_0 - B_1)\exp(-C_f \gamma_{(n)}^p) + B_1 \qquad (7)$$

where B_1 and B_0=material hardening parameters; C_f=material parameter; and $\gamma_{(n)}^p$=accumulated plastic shear strain between two sequential stress reversal points in the previous cycles.

After the stress state reached the phase transformation line, B follows the following hyperbolic relation:

$$B = B_0/(1 + \gamma_{(n)\max}^p/\gamma_r^p) \qquad (8)$$

where γ_r^p=reference plastic strain parameter.

In addition, the degradation of elastic shear modulus is also considered in a similar way

$$G^e = G_0^e/(1 + \gamma_{(n)\max}^e/\gamma_r^e) \qquad (9)$$

where γ_r^e=reference elastic strain parameter and G_0^e=initial value of the elastic shear modulus G^e.

As the nonassociated flow rule is used, the plastic potential function is expressed as follows:

$$g = \sqrt{(\eta_{ij} - \chi_{ij})(\eta_{ij} - \chi_{ij})} + \tilde{M} \ln(\sigma_m'/\sigma_{ma}') = 0 \qquad (10)$$

where σ_{ma}'=material constant and $\tilde{M}$=stress ratio when the maximum compression of the material takes place.

When $f_b \geq 0$, $\tilde{M}$ equals $M_{m'}$, otherwise it is defined as

$$\tilde{M} = -\sqrt{\eta_{ij}\eta_{ij}}/\ln(\sigma_m'/\sigma_{mc}') \qquad (11)$$

in which

$$\sigma_{mc}' = \sigma_{mb}' \exp(\sqrt{\eta_{ij(0)}\eta_{ij(0)}}/M_m) \qquad (12)$$

The stress-dilatancy relation is expressed by using the generalized flow rule as

$$d\nu^p/d\gamma^p = D(\tilde{M} - \eta_x) \qquad (13)$$

where $D = D_0(\tilde{M}/M_m)^n$ and $\eta_x = \eta_{ij}(\eta_{ij} - \chi_{ij})/\sqrt{(\eta_{mn} - \chi_{mn})(\eta_{mn} - \chi_{mn})}$. D_0 and n=dilatancy parameters.

References

Arulanandan, K., and Scott, R. F., eds. (1993). *VELACS: Verification of numerical procedures for the analysis of soil liquefaction problems*, Balkema, Rotterdam, The Netherlands.

Di, Y., and Sato, T. (2004). "A practical numerical method for large strain liquefaction analysis of saturated soils." *Soil Dyn. Earthquake Eng.*, 24(3), 251–260.

Elgamal, A., Parra, E., Yang, Z., and Adalier, K. (2002). "Numerical analysis of embankment foundation liquefaction countermeasures." *J. Earthquake Eng.*, 6(4), 447–471.

Fudo Construction Co. Ltd. (Fudo). (1994). *Investigation Rep. on the 1994 Hokkaido Toho-oki Earthquake* (in Japanese).

Hamada, M., Isoyama, R., and Wakamatsu, K. (1996). "Liquefaction-induced ground damage and its related damage to lifeline facilities." *Soils Found.*, Special Issue, 81–98.

Hamada, M., Yasuda, S., Isoyama, R., and Emoto, K. (1986). "Study on liquefaction induced permanent ground displacements." *Research Committee Rep.*, Association for the Development of Earthquake Prediction, Tokyo.

Liu, H. X., Housner, G. W., Xie, L. L., and He, D. (2002). "The Great Tangshan Earthquake of 1976." *Technical Rep.*, California Institute of Technology, Pasadena, Calif.

Matsuo, O. (1996). "Damage to river dikes." *Soils Found.*, 36(1), 235–240.

Matsuo, O., Shimazu, T., Uzuoka, R., Mihara, M., and Nishi, K. (2000). "Numerical analysis of seismic behavior of embankments founded on liquefiable soils." *Soils Found.*, 40(2), 21–39.

National Institute for Land and Infrastructure Management and Kiso-Jiban Consultants Co. Ltd. (NILIM-KJC). (2004). *Reconnaissance Rep. on Strong Ground Motion Records of River Embankments and Structures*, Tokyo, Japan (in Japanese).

Oka, F., Yashima, A., Shibata, T., Kato, M., and Uzuoka, R. (1994). "FEM-FDM coupled liquefaction analysis of a porous soil using an elastic-plastic model." *Appl. Sci. Res.*, 52(3), 209–245.

Oka, F., Yashima, A., Tateishi, A., Taguchi, Y., and Yamashita, S. (1999). "A cyclic elastic-plastic constitutive model for sand considering a plastic-strain dependence of the shear modulus." *Geotechnique*, 49(5), 661–680.

Okamura, M., Ishihara, M., and Oshita, T. (2003). "Liquefaction resistance of sand deposit improved with sand compaction piles." *Soils Found.*, 43(5), 175–187.

Sasaki, Y., Tamura, K., Yamamoto, M., and Ohbayashi, J. (1995). "Soil improvement work for river embankment damaged by the 1993 Kushiro-oki earthquake." *Proc., 1st Int. Conf. on Earthquake Geotechnical Engineering*, Balkema, Rotterdam, The Netherlands, 43–48.

Seed, H. B. (1970). "Soil problems and soil behaviour." *Earthquake engineering*, R. L. Wiegel, ed., Prentice-Hall Inc., Englewood Cliffs, N.J.

Yang, J., Sato, T., and Li, X. S. (2000). "Nonlinear site effects on strong ground motion at a reclaimed island." *Can. Geotech. J.*, 37(1), 26–39.